





Article

Sentinel-1 InSAR Measurements of Elevation Changes over Yedoma Uplands on Sobo-Sise Island, Lena Delta

Jie Chen ^{1,2,3,*} , Frank Günther ⁴ , Guido Grosse ^{4,5} , Lin Liu ²  and Hui Lin ^{1,3,6,*}

¹ Institute of Space and Earth Information Science, The Chinese University of Hong Kong, 999077 Hong Kong, China

² Earth System Science Programme, Faculty of Science, The Chinese University of Hong Kong, 999077 Hong Kong, China; liulin@cuhk.edu.hk

³ Shenzhen Research Institute, The Chinese University of Hong Kong, 518172 Shenzhen, China

⁴ Alfred Wegener Institute Helmholtz Centre for Polar and Marine Research, 14473 Potsdam, Germany; Frank.Guenther@awi.de (F.G.); guido.grosse@awi.de (G.G.)

⁵ Institute of Earth and Environmental Sciences, University of Potsdam, 14476 Potsdam, Germany

⁶ Department of Geography and Resource Management, The Chinese University of Hong Kong, 999077 Hong Kong, China

* Correspondence: jiechen@link.cuhk.edu.hk (J.C.); huilin@cuhk.edu.hk (H.L.); Tel.: +852-3943-1459 (J. C)

Received: 31 May 2018; Accepted: 20 July 2018; Published: 21 July 2018



Abstract: Yedoma—extremely ice-rich permafrost with massive ice wedges formed during the Late Pleistocene—is vulnerable to thawing and degradation under climate warming. Thawing of ice-rich Yedoma results in lowering of surface elevations. Quantitative knowledge about surface elevation changes helps us to understand the freeze-thaw processes of the active layer and the potential degradation of Yedoma deposits. In this study, we use C-band Sentinel-1 InSAR measurements to map the elevation changes over ice-rich Yedoma uplands on Sobo-Sise Island, Lena Delta with frequent revisit observations (as short as six or 12 days). We observe significant seasonal thaw subsidence during summer months and heterogeneous inter-annual elevation changes from 2016–17. We also observe interesting patterns of stronger seasonal thaw subsidence on elevated flat Yedoma uplands by comparing to the surrounding Yedoma slopes. Inter-annual analyses from 2016–17 suggest that our observed positive surface elevation changes are likely caused by the delayed progression of the thaw season in 2017, associated with mean annual air temperature fluctuations.

Keywords: Sentinel-1 InSAR; Yedoma uplands; Sobo-Sise Island; summer heave; permafrost thaw subsidence; active layer

1. Introduction

Yedoma—extremely ice-rich permafrost with massive ice wedges formed in extensive regions in northern Siberia, Alaska, and northwest Canada during the Late Pleistocene [1,2]—is vulnerable to thawing and degradation under climate warming. The thawing of ice-rich permafrost results in widespread thermokarst development, reshaping the landscape into Yedoma uplands and interconnected drained thermokarst lake [3,4]. Due to its syngenetic formation history, Yedoma deposits store large amounts of organic carbon which are vulnerable to mobilization upon thaw [5,6]. Therefore, Yedoma degradation contributes to climate warming through the release of greenhouse gases from microbial decomposition of thawed organic carbon [7,8].

Thermokarst and associated thaw subsidence are key land surface indicators for permafrost degradation processes [9]. To study surface elevation changes over ice-rich Yedoma, associated with the freeze and thaw cycling processes, is of importance to understand the response of Yedoma uplands to surface disturbance and/or climatic changes. Generally, the ground surface subsides/uplifts seasonally as a result of the volumetric contraction/expansion due to the moisture phase transition between the frozen and unfrozen soil in the active layer. In addition, upon surface disturbance, such as massive snowfall or precipitation, the volumetric ice content exceeds the total soil pore volume in freeze season, i.e., the formation of excess ground ice [10]. If the excess meltwater upon the thawing of excess ground ice in the uppermost permafrost layer is well drained, the ground experiences additional secular subsidence. Otherwise, the excess meltwater pools up and thus trigger the formation of the thermokarst landforms. The dynamic processes between the active layer and underlying ice-rich Yedoma deposits further affect soil moisture content and vegetation growth, leading to changes in ground thermal regime and the energy exchanges between the land surface and the atmosphere [11]. These interactions potentially provide further feedbacks to surface elevation changes.

Interferometric Synthetic Aperture Radar (InSAR) is a technique to quantify surface elevation changes independent of weather and light conditions, which is an ideal precondition for such studies in Arctic permafrost regions. The basic principle of InSAR for measuring deformation is to compare the phase of two complex Synthetic Aperture Radar (SAR) signals that were acquired from slightly different positions at different times. The phase differences are used to measure the displacements along the line of sight (LOS) between the repeat SAR acquisitions. InSAR measurements have been frequently used to measure ground surface subsidence for geophysical researches, such as deformation of volcanoes, earthquake-generated displacements, landslides, and urban studies [12–16].

The Sentinel-1A/B constellation is a new generation of two C-band SAR satellites, launched on 3 April 2014 and 25 April 2016, respectively. The main advancement of Sentinel-1 is the new imaging technique, i.e., the Terrain Observation by Progressive Scans (TOPS) [17]. This technique allows the Sentinel-1 SAR images to cover large footprints (about 250 km across the orbit track) by three overlapping sub-swaths. Sentinel-1 measurements characterize with frequent revisit time (regular revisit time is 12 days; shortest is six days if both Sentinel-1A and -1B images are acquired). Furthermore, the orbit configuration of Sentinel-1 results in a spatial baseline for InSAR of about 150 m [18]. The European Space Agency (ESA), operated Global Monitoring for Environment and Security (GMES) space component program, provides all the Sentinel-1A/B archives at no cost to all users.

However, the availability of suitable SAR images for InSAR measurements not only relies on the revisit time of SAR missions but also highly depends on the interferometric coherence. Interferometric coherence, the similarity between the two SAR signals, is a key indicator of the quality of InSAR measurements. Generally, high interferometric coherence indicates that the phase observations contain useful information and are less affected by noise. The source of decorrelation (loss of coherence) is mainly related to the variation of geometric configuration between the repeat-pass satellites, the temporal variation in the physical features of the ground surface, and the thermal noise [19,20]. The geometric decorrelation is related to the satellite configurations (i.e., incident angle, wavelength, spatial resolution, and satellite to ground distance) and the spatial baseline between repeat satellite observations. Taking the maximum spatial baseline (about 150 m) as an example, the spatial correlation term is about 0.96, suggesting that the geometric decorrelation for Sentinel-1 InSAR can be ignored [18]. Hence, the dominant decorrelation source is the temporal decorrelation related to surface processes, mainly including soil moisture variation, freezing and thawing processes, and vegetation phenology changes and succession.

The space-borne X-band, C-band, and L-band repeat-pass SAR missions prior to the Sentinel-1A/B satellites have been used to monitor seasonal and inter-annual thaw subsidence in permafrost regions [21–24]. However, these InSAR measurements (C- and L-band) only provide a limited number of repeat images, and hardly resolve the temporal evolution of seasonal thaw subsidence and/or inter-annual variabilities. TerraSAR-X, the X-band repeat-pass SAR mission, provides frequent measurements (regular revisit time is 11 days). TerraSAR-X InSAR measurements have a high sensitivity to changes at the ground surface [25–27]. Thus, the interferometric coherence of X-band data drops rapidly through time in tundra lowlands, which limits the suitability of X-band repeat-pass SAR to detect thaw subsidence [28]. The Sentinel-1 InSAR measurements with relatively high temporal resolution provide an excellent opportunity to study the suitability of C-band data for permafrost elevation changes in a detailed manner.

The aim of this study is to demonstrate the capability of Sentinel-1 InSAR measurements to detect elevation changes over Yedoma uplands in an Arctic permafrost region. We use the InSAR approach to quantify the seasonal and inter-annual elevation changes over ice-rich Yedoma uplands on Sobo-Sise Island, Lena Delta. To understand the spatial patterns of seasonal subsidence, we analyze the correlation between seasonal thaw subsidence and Yedoma elevation. To account for the temporal evolution of inter-annual elevation changes, we also analyze the relationship between the inter-annual elevation changes and air temperature.

2. Datasets and Methods

2.1. Study Site

Sobo-Sise Island is located between two Lena River channels (Sardakhsкая and Bykovskaya channels) in the southeastern Lena River Delta, adjacent to the Laptev Sea (Figure 1a). According to Reference [3], Sobo-Sise Island belongs to the third geomorphological terrace of the Lena Delta, that is characterized by remnants of Yedoma deposits with large syngenetic ice wedges and hence high ice content [29]. This island is largely occupied by Yedoma uplands as well as permafrost degradation landforms, such as thermokarst lakes, drained thaw lake basins, and thermal erosion gullies [3]. The total area of Sobo-Sise is about 340 km², accounting for 16% of the Yedoma coverage in the Lena Delta. Fuchs et al. [30] classified and mapped different landforms (Yedoma uplands, thermokarst basins, water bodies, etc.) based on RapidEye satellite imagery. As we focus on Yedoma uplands, we mask out the thermokarst basins and water bodies using this geomorphological classification [30]. Our study domain on Sobo-Sise thus consists of the classes flat undisturbed Yedoma uplands and partly degraded Yedoma slopes from [30]. The elevation of Yedoma uplands reaches about 35 m above the sea level (Figure 1b).

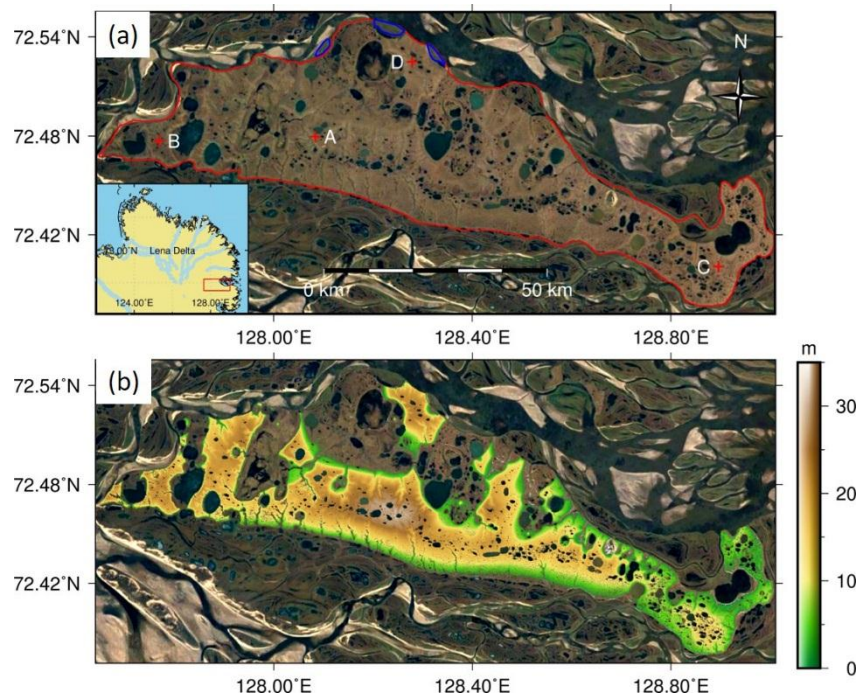


Figure 1. (a) Google Earth Image of Sobo-Sise Island. The red polygon outlines the island. The red crosses mark the four positions for which we present the results from InSAR time-series analysis. The three blue polygons are used to calibrate the InSAR measurements. The inset shows the location of Sobo-Sise Island in the southeastern Lena River Delta. (b) Elevation above the mean sea level over the Yedoma uplands and slopes. Thermokarst basins and water bodies are masked out.

The closest weather station, located at Samoylov Island about 50 km to the southwest of Sobo-Sise Island, has collected meteorological data since 1998 [31]. The weather is characterized by extremely cold winters with temperatures around $-30\text{ }^{\circ}\text{C}$ generally in January and February and highest temperatures around $10\text{ }^{\circ}\text{C}$ in July and August. The mean annual air temperature is about $-12.5\text{ }^{\circ}\text{C}$ and the annual precipitation is in a range of 180–200 mm. Snowmelt usually begins in May and lasts until early to mid-June; by that time, the soil begins to thaw, and the highest thaw rates are recorded in June and July. The maximum thaw depth is reached in late August to early September and snowfall typically starts from early to mid-September. The vegetation coverage is sparse and characterized by moist to wet sedge- and moss-dominated tundra [32]. The vegetation growth period lasts from June to September and is roughly similar to the thaw season [30]. The maximum active layer thickness ranges from 20 cm to 50 cm on the Yedoma uplands.

2.2. TanDEM-X Digital Elevation Model

TanDEM-X (TerraSAR-X add-on for Digital Elevation Measurement) mission provides a global digital elevation model (DEM) product based on bistatic single-pass InSAR measurements [33]. The absolute vertical height accuracy of the TanDEM-X DEM is less than 10 m, whereas the relative height accuracy is about 3 m globally [34]. In this study, we utilize the standard DEM product with a spatial resolution of about 12 m to remove the topographic phase contribution in our InSAR time-series processing. Figure 1b shows the TanDEM-X DEM over the Yedoma uplands.

2.3. Sentinel-1 InSAR Processing

We selected 14 descending Sentinel-1A/B images (6 scenes in 2016 and 8 scenes in 2017, interferometric wide swath mode) taken from the thaw seasons (late June–September). There were no ascending Sentinel-1 images of the same observation mode acquired over this region, therefore none

were used in this study. Snow cover would alter the phase center corresponding to SAR images acquired in winter seasons and cause severe decorrelation [35], making the interferograms less reliable, therefore they were not adopted in this study. The acquisition dates and platforms for SAR image acquisitions are listed in Table 1.

Table 1. The acquisition date and platform of SAR images used in this study.

Acquisition Date (yyyymmdd)	Platform
20160722	Sentinel-1A
20160803	Sentinel-1A
20160815	Sentinel-1A
20160827	Sentinel-1A
20160908	Sentinel-1A
20160926	Sentinel-1B
20170617	Sentinel-1B
20170711	Sentinel-1B
20170723	Sentinel-1B
20170804	Sentinel-1B
20170816	Sentinel-1B
20170828	Sentinel-1B
20170909	Sentinel-1B
20170921	Sentinel-1B

We constructed one-season image pairs between any two SAR acquisitions in the thaw season of 2016 and 2017, separately. We excluded image pairs with time intervals exceeding 48 days to avoid severe temporal decorrelation. To exploit the inter-annual elevation changes between two thaw seasons, we also constructed the two-season image pairs with 366 days span. Then, we generated the interferograms for the selected image pairs using the InSAR Scientific Computing Environment (ISCE) [36]. We utilized the TanDEM-X DEM product to evaluate and remove the topographic phase of each interferogram. We further excluded the interferograms with low coherence and/or the ones accompanied by strong atmospheric artifacts. The perpendicular and temporal baselines of the selected 32 interferograms are presented in Figure 2. The largest spatial baseline is on the order of 150 m. Finally, we unwrapped the interferograms using the minimum cost flow approach [37].

We calibrated our interferograms by selecting three regions that we knew from field studies or high-resolution imagery where dominated by sandy deposits. The locations of the three sites are outlined by blue polygons in Figure 1a. We expect that these sites contain a low ground ice content and are well drained, and thus experience no or very limited elevation changes during 2016–17. We then averaged the interferometric phase for these sites, serving as the reference value, and subtracted it from each individual interferogram. Therefore, reported elevation changes in our study were relative to the reference value. We noted that the estimated elevation changes were along the slant LOS direction. Because the Yedoma uplands were flat, we assumed that vertical movement dominates the deformation. Therefore, LOS deformation rates were converted to the vertical direction by simply dividing by the cosine of the incidence angle.

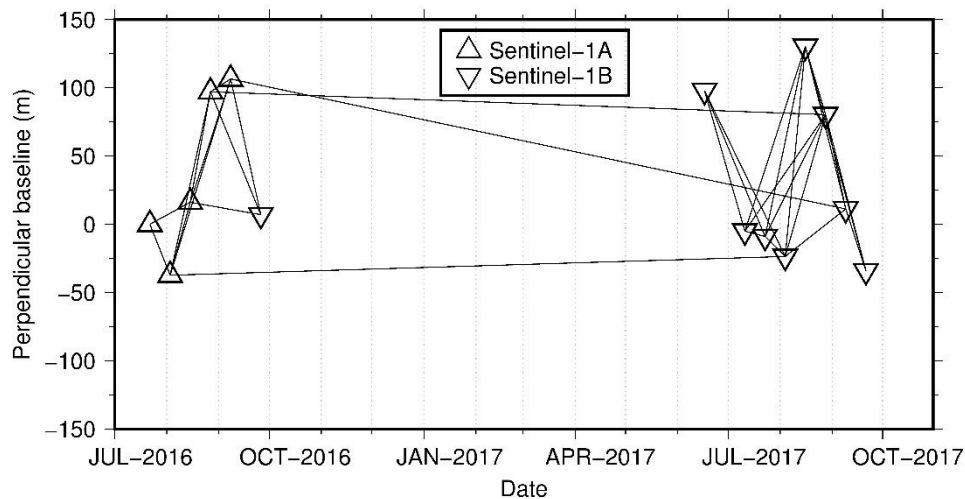


Figure 2. The connections between 12 Sentinel-1A/B SAR images with the perpendicular and temporal baselines.

We retrieved time series of elevation changes for each coherent pixel based on the small baseline approach. The small baseline approach was proposed to derive the independent deformation with respect to each acquisition time from a set of redundant interferograms [38]. The well-developed Generic InSAR Analysis Toolbox (GIAnt) [39] was used to derive the time series of surface elevation changes in our study. We removed the possible orbital ramps prior to the time-series analysis, using the network de-ramping approach [40]. With each SAR acquisition time, we obtained the elevation changes relative to the first SAR acquisition.

According to the air temperature records, we determined the thawing and freezing onset as 13 June and 7 September in 2017, respectively. Then, we calculated the elevation changes between 17 June and 9 September to account for accumulated seasonal thaw subsidence in 2017. The thawing onset began on 28 May in 2016, which was about half a month earlier than in 2017. Due to no available Sentinel-1 SAR images between 28 May and 22 July in 2016, we could not obtain the maximum seasonal thaw subsidence in 2016. To evaluate the inter-annual elevation changes, we calculated the averaged elevation changes between the five inter-annual image pairs with 366-days interval from the thaw season of 2016 and 2017.

3. Results

3.1. Accumulated Subsidence in the Thaw Season of 2017

The InSAR measurements show that all the Yedoma uplands undergo ground subsidence in the thaw season of 2017. The accumulated subsidence between 17 June and 9 September in 2017 of up to 2–3 cm is most pronounced on top of flat Yedoma uplands (Figure 3). The eastern regions, as well as the outer boundaries of the Yedoma uplands with lower elevation, experience less subsidence (0.5–1.0 cm).

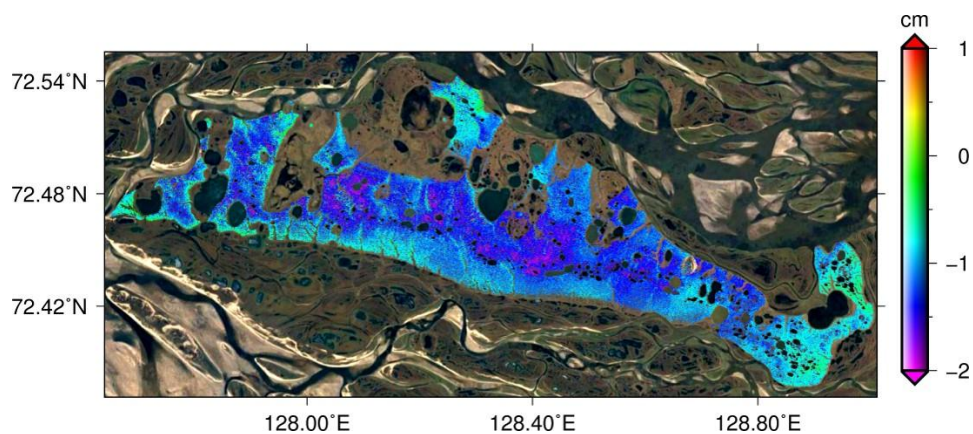


Figure 3. Surface elevation changes over the Yedoma uplands on Sobu-Sise Island from 23 June to 9 September in 2017. Minus values denote ground subsidence.

To further exploit the relationship between Yedoma elevation and seasonal subsidence, we averaged subsidence magnitudes in each 5 m elevation interval (Figure 4). The seasonal subsidence in different Yedoma height bins reveals exclusively negative changes over time. Stronger subsidence signals on top of Yedoma uplands and less pronounced subsidence are found on upland-surrounding slopes. According to the range of subsidence magnitudes at each elevation bin, the variability of height changes is less pronounced at elevations larger than 25 m.

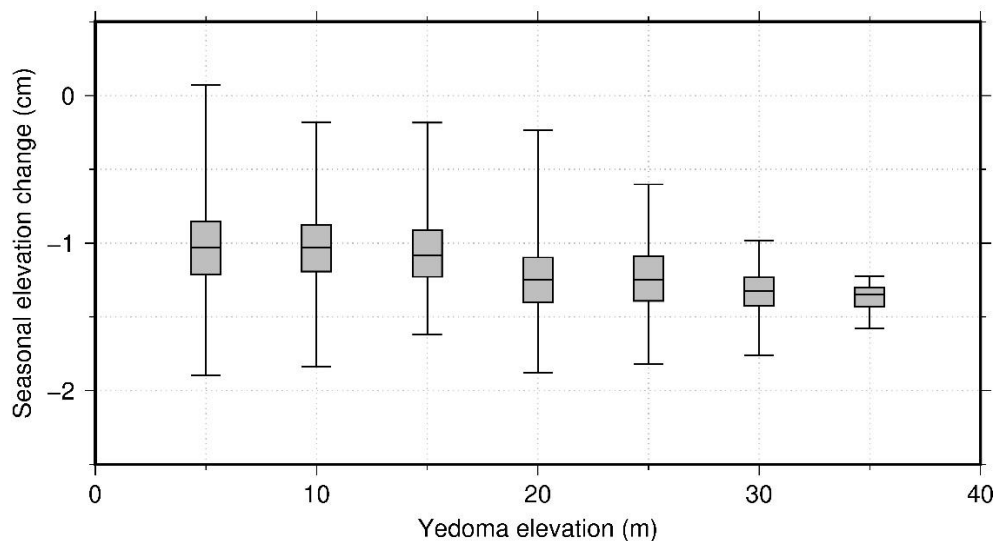


Figure 4. Box plot (minimum, first quartile, median, third quartile, maximum) for seasonal subsidence at different Yedoma elevations during the thaw season of 2017.

3.2. Inter-Annual Elevation Changes

The averaged inter-annual elevation changes show almost exclusively positive values in most of the Yedoma uplands (Figure 5). This suggested the averaged ground subsidence during the thaw season of 2017 is less intense when compared with the preceding year 2016 and results mostly in an overall positive net inter-annual elevation changes of up to 1 cm from late thaw season 2016–17.

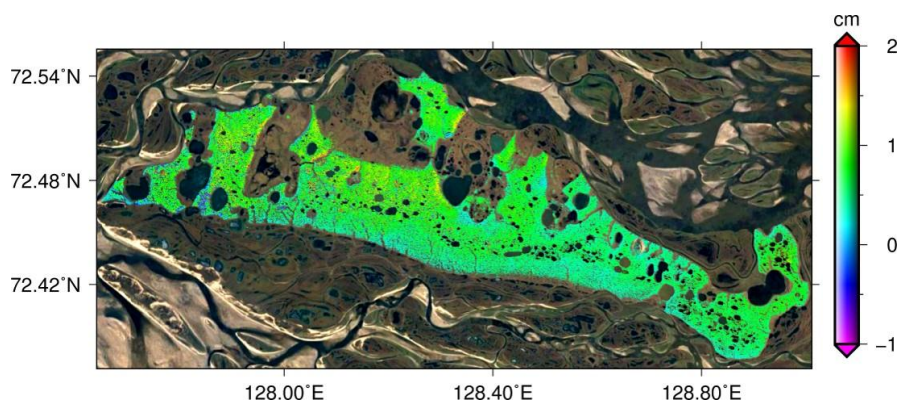


Figure 5. Averaged inter-annual elevation changes between the late thaw seasons of 2016 and 2017.

To characterize the temporal evolution of the net inter-annual uplift, we calculated the corresponding elevation changes from six individual image pairs with 366 days interval between 2016 and 2017 (Figure 6). The net inter-annual uplift reaches its maximum values of up to 2 cm at the beginning of August comparing to the preceding 2016. The relative uplift drops rapidly and becomes zero or turns even into subsidence at about -0.5 cm on 9 September 2017 compared to 8 September 2016. Then, the uplift appeared again on 21 September 2017 compared to 26 September 2016.

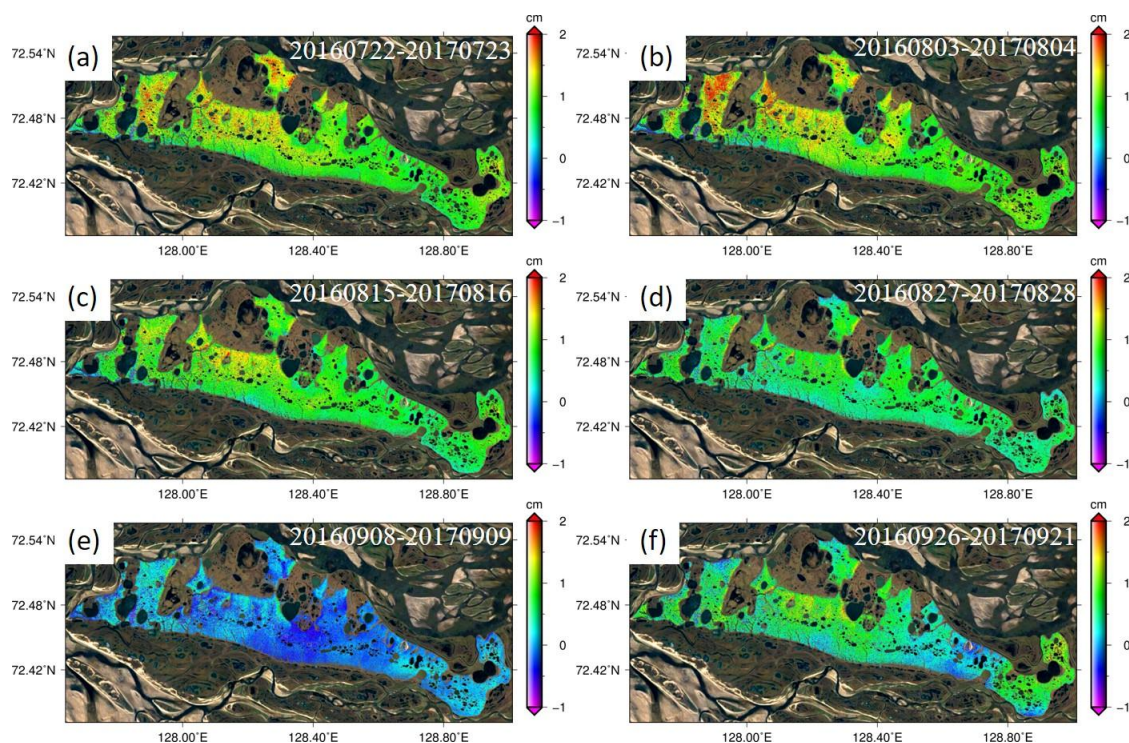


Figure 6. Inter-annual elevation changes between image pairs (a) 20160722–20170723 (b) 20160803–20170804; (c) 20160815–20170816; (d) 20160827–20170828; (e) 20160908–20170909 and (f) 20160926–20170921.

3.3. Time-Series Analysis of Elevation Changes

We selected four points to demonstrate the time series of elevation changes and their spatial variations derived from InSAR. The ground undergoes limited negative elevation changes between early August and the end of thaw season in 2016 (Figure 7). The ground shows stronger subsidence in

2017 comparing to the same period in 2016. However, the ground begins to uplift around 0.5–1 cm during the early thaw season in 2017. Then, the ground turns to subside around 23 July 2017 and this seasonal subsidence period ends around 9 September 2017. Finally, ground uplift is detected again on 21 September 2017.

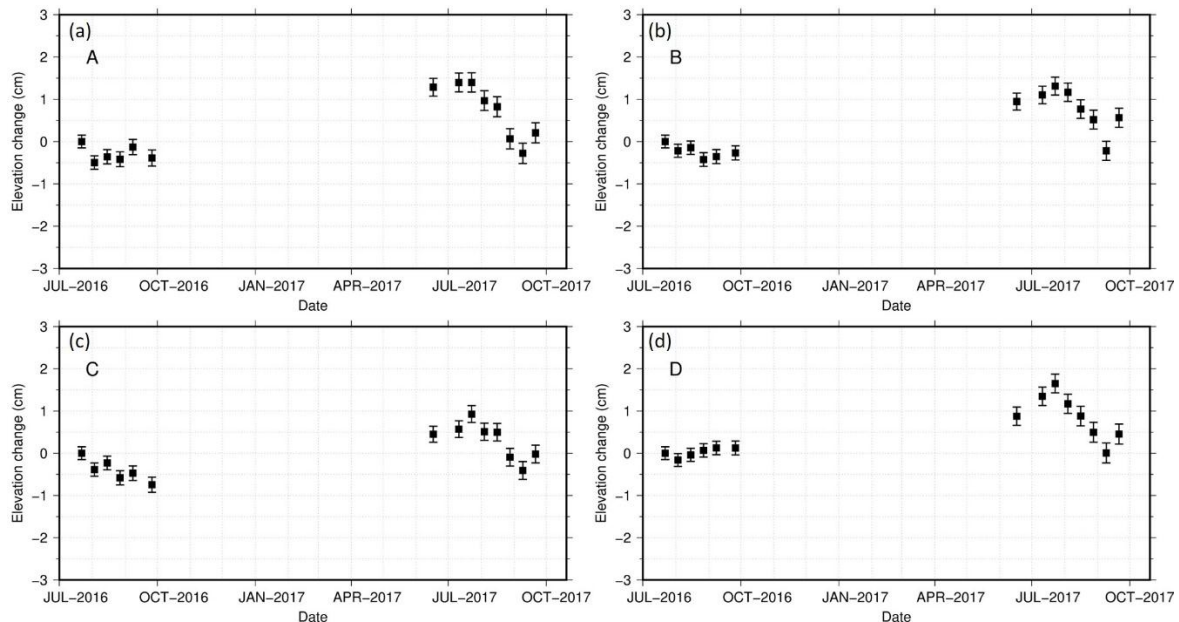


Figure 7. Time series of elevation changes based on our InSAR measurements at points (a) A; (b) B; (c) C; (d) D relative to the first acquisition on 22 July 2016. The error bars denote the uncertainty of the InSAR time series. The locations of the four points are shown in Figure 1.

4. Discussion

4.1. The Capability of Sentinel-1 InSAR over Permafrost Regions

Sentinel-1 InSAR measurements are capable of capturing both the seasonal thaw subsidence, as well as the inter-annual elevation changes in a permafrost environment. This study benefits from the availability of more InSAR measurements with sufficient coherence in one thaw season and across two thaw seasons. Sentinel-1 InSAR measurements provide an excellent opportunity to identify permafrost-related elevation changes in a detailed manner and therefore help towards a better understanding of the dynamic land surface processes in an ice-rich permafrost region.

The interferometric coherence for all the possible image pairs in 2017 over the Yedoma uplands is shown in Figure A1 (in Appendix A). The 12-days interferograms present relatively low coherence at the beginning (image pair 20170716–20170729) and the ending of the thaw season (image pair 20170909–20170921), whereas the 12-days interferograms in July and August present relatively higher coherence. Antonova et al. [25,28] utilized X-band TerraSAR images to detect elevation changes over Kurungnakh-Sise Island, around 50 km away from Sobo-Sise Island. The Yedoma deposits there are of the same origin as at our study site. In contrast to our study, they observed a relatively high coherence at the beginning and ending of the thaw season based on 11-days interferograms acquired from TerraSAR-X images. This might be related to the different sensitivity of X-band and C-band to the thawing and freezing processes. Furthermore, the X-band interferograms with time intervals of more than 22 days show severe decorrelation, when our Sentinel-1 interferograms present moderate coherence even for 48-days intervals or more (Figure 8). Better coherence, especially with relatively long temporal baseline, makes the C-band Sentinel-1 InSAR prevail over X-band InSAR in capturing surface elevation changes in permafrost regions.

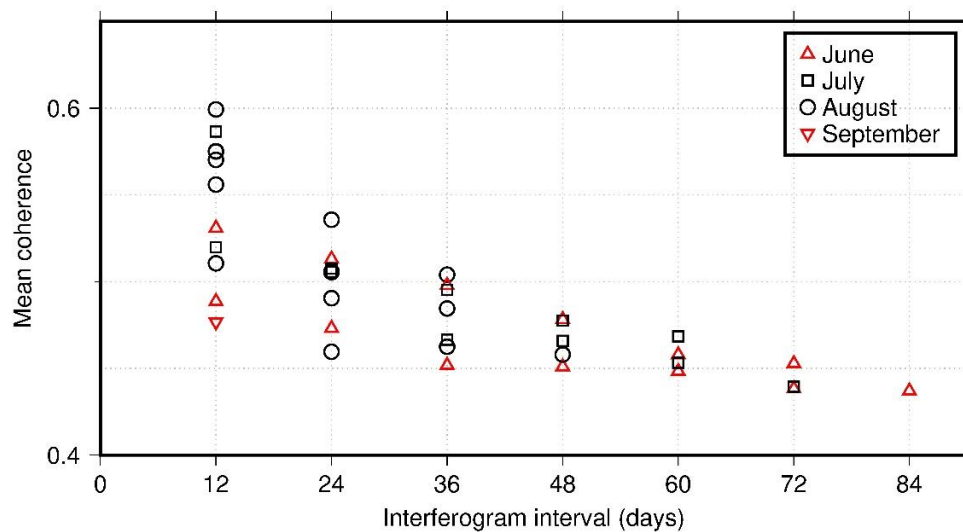


Figure 8. Mean coherence over the Yedoma upland for all the 2017 interferograms. The legend symbols denote the months of the master images used to construct the interferograms.

4.2. Correlation between Yedoma Elevation and Seasonal Thaw Subsidence

We find that the highest flat Yedoma uplands, i.e., the undisturbed regions, present the highest seasonal thaw subsidence in 2017. Typically, the water/ice content in the active layer predominantly accounts for the seasonal elevation changes. The active layer thickness does not significantly vary among the Yedoma uplands [30]. Thus, the highest subsidence amplitudes over the top of Yedoma uplands suggest higher water/ice contents than in lower regions. While the soil organic layer acts as a protective layer slowing the thaw and degradation of underlying permafrost, the thickness of such insulating organic layers is generally rather small (<10 cm) on Yedoma uplands. However, radiocarbon dating of four Yedoma upland cores by Reference [30] demonstrated that even at a depth of 233 cm ice complex Yedoma deposits in a narrower sense were still overlain by the Holocene soil cover. This suggests that even on top of the Yedoma uplands very ice-rich deposits were reached only at greater depth, but with volumetric ice contents of $61.5 \pm 15\%$, the Holocene cover was still prone to thaw and degradation and thus subsequent thaw subsidence processes. However, strong exposure to wind removes snow from uplands and thus limits winter insulation by snow, effectively cooling and preserving near-surface permafrost on Yedoma uplands. A key parameter for upland degradation and thaw subsidence potential seems to be availability and size of flat areas with poor drainage conditions, where subsidence and subsequent positive feedbacks such as water ponding and increases in snow thickness may happen, leading to thermokarst.

4.3. Temporal Evolution of Elevation Changes

The net inter-annual uplift from late season 2016–17 observed was possibly caused by delayed thawing associated with differences in summer air temperatures. We downloaded the air temperature and snow cover records from a meteorological station located on Stolb Island, about 40 km west of Sobo-Sise Island (https://rp5.ru/Weather_in_the_world). According to the air temperature records, degree days of thawing (days) in 2016 were 812, and in 2017 only 667. We also observed a shift of the warmest month from typically July to August (Figure 9). Mean air temperature in July 2016 was 7.8 °C and in August was 7.3 °C. In 2017, July temperature was only 7.2 °C, while August was warmer at 8.3 °C. Even more pronounced were differences between September 2016 and 2017 (164 vs. 63 degree days of thawing). These support our observation of higher surface elevations in 2017 compared to those at the same time in 2016. However, the 20160908–20170909 image pair in Figure 6 suggests that elevation changes turn into inter-annual thaw subsidence later at the end of the 2017 thaw

season. The apparent pseudo-uplift between the thaw seasons in 2016 and 2017, therefore, reflects a delay in progression of the thaw season and implies that seasonal thaw settlement may not develop simultaneously when compared to the preceding year. This also suggests that it is not appropriate to estimate the inter-annual subsidence by simply averaging the elevation changes. A detailed assessment of meteorological and permafrost conditions for the analyzed years should be necessary to interpret the actual evolution of elevation change dynamics.

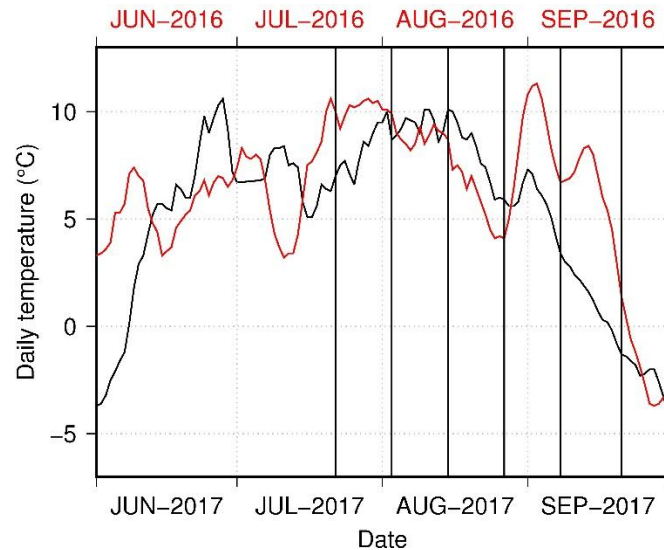


Figure 9. Daily air temperature for the thaw season of 2016 (red) and 2017 (black). The six vertical solid lines denote the dates of the inter-annual SAR acquisition pairs.

The InSAR-derived elevation changes show obvious uplift in the early thaw season of 2017. This might be due to the so-called summer heave. In early thaw season, excess water (for instance, rain, snowmelt, and groundwater flow) could penetrate into the underlying frozen active layer and even the adjacent permafrost and refreeze. Mackay et al. [41] observed summer frost heave up to 1 cm at Garry Island, Canada, from five years of field measurements. According to the relatively thicker snow accumulation in the winter season between 2016 and 2017, the excess snowmelt water makes the ground more prone to undergo summer heave. Furthermore, the downward water movement makes the frozen ground saturated or oversaturated and thus needs more heat flux to thaw, which further supports the likely delay of thaw season in 2017. However, Zwieback et al. [42] reported that the post-snowmelt drying processes would potentially change the dielectric property of the ground surface and thus contribute to the uplift-like signal in L-band InSAR. Because the sensitivity of C-band Sentinel-1 InSAR to changes of dielectric properties is still not well determined and no in situ soil moisture measurements were conducted in our study area, so at this point we cannot determine if the uplift is spurious. Evidence of ice and snow suggests that penetration depth depends on carrier frequency, physical and electrical characteristics which may vary according to climate conditions [43]. To account for the observed uplift within one thaw season, further efforts should focus on the question to what extent the soil moisture variations affects InSAR observations.

5. Conclusions

We explored and successfully tested the capability of Sentinel-1 InSAR measurements for quantifying both permafrost thaw subsidence during one thaw season and the inter-annual elevation changes between two thaw seasons. Compared with X-band InSAR in Yedoma uplands, the C-band Sentinel-1 InSAR shows higher coherence, even for the interferograms between the years. We found that the flat tops of Yedoma uplands exhibit the highest seasonal elevation changes. Benefitting from

the Sentinel-1 InSAR measurements with short time intervals (12 days in this case), we found that delayed thawing associated with air temperature fluctuations affects inter-annual elevation changes. We also observed an uplift in the early season of 2017, which may relate to effects of early summer heave or soil moisture impacts. To discriminate these and to better interpret the InSAR-derived elevation changes, further research should focus on impacts of soil moisture variation on InSAR measurements. Our study suggests that the Sentinel-1 InSAR measurements with high temporal resolution are capable of detecting permafrost-related elevation changes in a detailed manner and therefore help to better understand the land surface dynamics in an ice-rich permafrost region.

Author Contributions: J.C., F.G., G.G., L.L., and H.L. conceived and designed this study. J.C. conducted the data processing and analysis. J.C. and F.G. wrote the manuscript with contributions from all the authors. F.G., G.G., L.L., and H.L. helped to analyze and interpret the InSAR measurements.

Acknowledgments: The Sentinel-1 SAR data was downloaded from the Alaska Satellite Facility (<https://www.asf.alaska.edu/sentinel/>). The TanDEM-X DEM product was provided by the German Aerospace Center (DLR). Jie Chen, Lin Liu, and Hui Lin were supported by the National Key Basic Research Program of China 2015CB954103, the Hong Kong Research Grants Council projects CUHK14233016, CUHK24300414 and G-CUHK403/15. Frank Günther and Guido Grosse were supported by DAAD #57216164 within the PPP Hong Kong program, ERC PETA-CARB #338335, and ESA GlobPermafrost.

Conflicts of Interest: The authors declare no conflicts of interest.

Appendix A

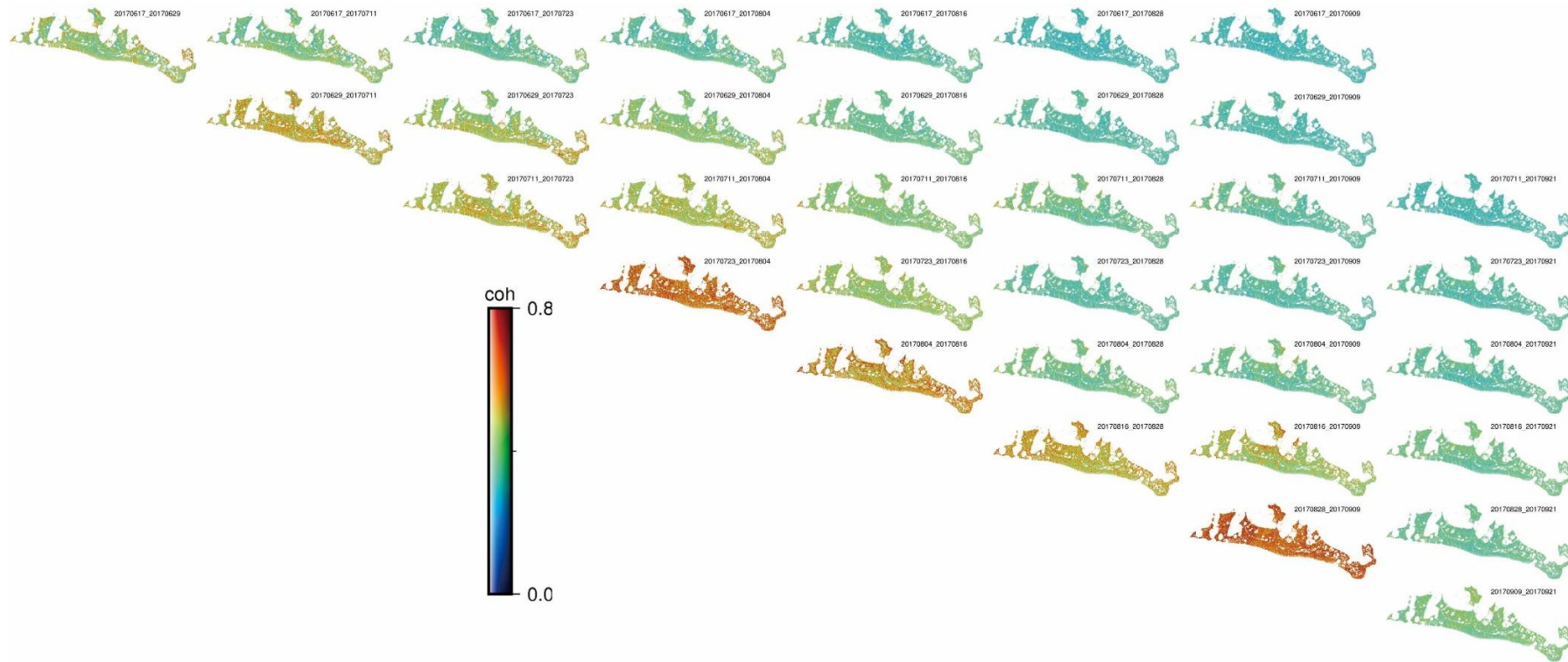


Figure A1. All the possible coherence maps for the thaw season of 2017.

References

- Schirrmeister, L.; Kunitsky, V.; Grosse, G.; Wetterich, S.; Meyer, H.; Schwamborn, G.; Babiy, O.; Derevyagin, A.; Siegert, C. Sedimentary characteristics and origin of the Late Pleistocene Ice Complex on north-east Siberian Arctic coastal lowlands and islands—A review. *Quat. Int.* **2011**, *241*, 3–25. [CrossRef]
- Schirrmeister, L.; Froese, D.; Tumskoy, V.; Grosse, G.; Wetterich, S. Yedoma: Late Pleistocene Ice-Rich Syngenetic Permafrost of Beringia A2—Elias, Scott A. In *Encyclopedia of Quaternary Science*, 2nd ed.; Mock, C.J., Ed.; Elsevier: Amsterdam, The Netherlands, 2013; pp. 542–552.
- Morgenstern, A.; Grosse, G.; Günther, F.; Fedorova, I.; Schirrmeister, L. Spatial analyses of thermokarst lakes and basins in Yedoma landscapes of the Lena Delta. *Cryosphere* **2011**, *5*, 849–867. [CrossRef]
- Ulrich, M.; Grosse, G.; Strauss, J.; Schirrmeister, L. Quantifying Wedge-Ice Volumes in Yedoma and Thermokarst Basin Deposits. *Permafr. Periglac. Process.* **2014**, *25*, 151–161. [CrossRef]
- Hugelius, G.; Strauss, J.; Zubrzycki, S.; Harden, J.W.; Schuur, E.A.G.; Ping, C.L.; Schirrmeister, L.; Grosse, G.; Michaelson, G.J.; Koven, C.D.; et al. Estimated stocks of circumpolar permafrost carbon with quantified uncertainty ranges and identified data gaps. *Biogeosciences* **2014**, *11*, 6573–6593. [CrossRef]
- Strauss, J.; Schirrmeister, L.; Grosse, G.; Fortier, D.; Hugelius, G.; Knoblauch, C.; Romanovsky, V.; Schädel, C.; Schneider von Deimling, T.; Schuur, E.A.G.; et al. Deep Yedoma permafrost: A synthesis of depositional characteristics and carbon vulnerability. *Earth-Sci. Rev.* **2017**, *172* (Suppl. C), 75–86. [CrossRef]
- Schuur, E.A.G.; McGuire, A.D.; Schadel, C.; Grosse, G.; Harden, J.W.; Hayes, D.J.; Hugelius, G.; Koven, C.D.; Kuhry, P.; Lawrence, D.M.; et al. Climate change and the permafrost carbon feedback. *Nature* **2015**, *520*, 171–179. [CrossRef] [PubMed]
- Walter Anthony, K.; Daanen, R.; Anthony, P.; Schneider von Deimling, T.; Ping, C.-L.; Chanton, J.P.; Grosse, G. Methane emissions proportional to permafrost carbon thawed in Arctic lakes since the 1950s. *Nat. Geosci.* **2016**, *9*, 679–682. [CrossRef]
- Kokelj, S.V.; Jorgenson, M.T. Advances in Thermokarst Research. *Permafr. Periglac. Process.* **2013**, *24*, 108–119. [CrossRef]
- Van Everdingen, R.O. *Multi-Language Glossary of Permafrost and Related Ground-Ice Terms*; National Snow and Ice Data Center: Boulder, CO, USA, 1998; Available online: <http://nsidc.org/fgdc/glossary> (accessed on 20 August 2015).
- Shiklomanov, N.I.; Streletskiy, D.A.; Nelson, F.E.; Hollister, R.D.; Romanovsky, V.E.; Tweedie, C.E.; Bockheim, J.G.; Brown, J. Decadal variations of active-layer thickness in moisture-controlled landscapes, Barrow, Alaska. *J. Geophys. Res. Biogeosci.* **2010**, *115*, G00I04. [CrossRef]
- González, P.J.; Bagnardi, M.; Hooper, A.J.; Larsen, Y.; Marinkovic, P.; Samsonov, S.V.; Wright, T.J. The 2014–2015 eruption of Fogo volcano: Geodetic modeling of Sentinel-1 TOPS interferometry. *Geophys. Res. Lett.* **2015**, *42*, 9239–9246. [CrossRef]
- Grandin, R.; Klein, E.; Métois, M.; Vigny, C. Three-dimensional displacement field of the 2015 Mw8.3 Illapel earthquake (Chile) from across- and along-track Sentinel-1 TOPS interferometry. *Geophys. Res. Lett.* **2016**, *43*, 2552–2561. [CrossRef]
- Shirzaei, M.; Bürgmann, R.; Fielding, E.J. Applicability of Sentinel-1 Terrain Observation by Progressive Scans multitemporal interferometry for monitoring slow ground motions in the San Francisco Bay Area. *Geophys. Res. Lett.* **2017**, *44*, 2733–2742. [CrossRef]
- Dai, K.; Li, Z.; Tomás, R.; Liu, G.; Yu, B.; Wang, X.; Cheng, H.; Chen, J.; Stockamp, J. Monitoring activity at the Daguangbao mega-landslide (China) using Sentinel-1 TOPS time series interferometry. *Remote Sens. Environ.* **2016**, *186*, 501–513. [CrossRef]
- Sowter, A.; Bin Che Amat, M.; Cigna, F.; Marsh, S.; Athab, A.; Alshammari, L. Mexico City land subsidence in 2014–2015 with Sentinel-1 IW TOPS: Results using the Intermittent SBAS (ISBAS) technique. *Int. J. Appl. Earth Observ. Geoinf.* **2016**, *52*, 230–242. [CrossRef]
- De Zan, F.; Monti Guarnieri, A. TOPSAR: Terrain Observation by Progressive Scans. *IEEE Trans. Geosci. Remote Sens.* **2006**, *44*, 2352–2360. [CrossRef]
- Yagüe-Martínez, N.; Prats-Iraola, P.; González, F.R.; Bricc, R.; Shau, R.; Geudtner, D.; Eineder, M.; Bamler, R. Interferometric Processing of Sentinel-1 TOPS Data. *IEEE Trans. Geosci. Remote Sens.* **2016**, *54*, 2220–2234. [CrossRef]

19. Zebker, H.A.; Villasenor, J. Decorrelation in interferometric radar echoes. *IEEE Trans. Geosci. Remote Sens.* **1992**, *30*, 950–959. [[CrossRef](#)]
20. Bamler, R.; Just, D.; Center, G.R.S.D. Phase statistics and decorrelation in SAR interferograms. *System* **1995**, *1*, E2.
21. Liu, L.; Schaefer, K.M.; Chen, A.C.; Gusmeroli, A.; Zebker, H.A.; Zhang, T. Remote sensing measurements of thermokarst subsidence using InSAR. *J. Geophys. Res. Earth Surface* **2015**, *120*, 1935–1948. [[CrossRef](#)]
22. Liu, L.; Zhang, T.; Wahr, J. InSAR measurements of surface deformation over permafrost on the North Slope of Alaska. *J. Geophys. Res.-Earth* **2010**, *115*, F3. [[CrossRef](#)]
23. Short, N.; Brisco, B.; Couture, N.; Pollard, W.; Murnaghan, K.; Budkewitsch, P. A comparison of TerraSAR-X, RADARSAT-2 and ALOS-PALSAR interferometry for monitoring permafrost environments, case study from Herschel Island, Canada. *Remote Sens. Environ.* **2011**, *115*, 3491–3506. [[CrossRef](#)]
24. Daout, S.; Doin, M.-P.; Peltzer, G.; Socquet, A.; Lasserre, C. Large-scale InSAR monitoring of permafrost freeze-thaw cycles on the Tibetan Plateau. *Geophys. Res. Lett.* **2017**, *44*, 901–909. [[CrossRef](#)]
25. Antonova, S.; Kääh, A.; Heim, B.; Langer, M.; Boike, J. Spatio-temporal variability of X-band radar backscatter and coherence over the Lena River Delta, Siberia. *Remote Sens. Environ.* **2016**, *182*, 169–191. [[CrossRef](#)]
26. Zwieback, S.; Liu, X.; Antonova, S.; Heim, B.; Bartsch, A.; Boike, J.; Hajnsek, I. A Statistical Test of Phase Closure to Detect Influences on DInSAR Deformation Estimates Besides Displacements and Decorrelation Noise: Two Case Studies in High-Latitude Regions. *IEEE Trans. Geosci. Remote Sens.* **2016**, *54*, 5588–5601. [[CrossRef](#)]
27. De Zan, F.; Parizzi, A.; Prats-Iraola, P.; Lopez-Dekker, P. A SAR Interferometric Model for Soil Moisture. *IEEE Trans. Geosci. Remote Sens.* **2014**, *52*, 418–425. [[CrossRef](#)]
28. Antonova, S.; Sudhaus, H.; Strozzi, T.; Zwieback, S.; Kääh, A.; Heim, B.; Langer, M.; Bornemann, N.; Boike, J. Thaw Subsidence of a Yedoma Landscape in Northern Siberia, Measured In Situ and Estimated from TerraSAR-X Interferometry. *Remote Sens.* **2018**, *10*, 494. [[CrossRef](#)]
29. Schwamborn, G.; Rachold, V.; Grigoriev, M.N. Late Quaternary sedimentation history of the Lena Delta. *Quat. Int.* **2002**, *89*, 119–134. [[CrossRef](#)]
30. Fuchs, M.; Grosse, G.; Strauss, J.; Günther, F.; Grigoriev, M.; Maximov, G.M.; Hugelius, G. Carbon and nitrogen pools in thermokarst-affected permafrost landscapes in Arctic Siberia. *Biogeosciences* **2018**, *15*, 953–971. [[CrossRef](#)]
31. Boike, J.; Kattenstroth, B.; Abramova, K.; Bornemann, N.; Chetverova, A.; Fedorova, I.; Fröb, K.; Grigoriev, M.; Grüber, M.; Kutzbach, L.; et al. Baseline characteristics of climate, permafrost and land cover from a new permafrost observatory in the Lena River Delta, Siberia (1998–2011). *Biogeosciences* **2013**, *10*, 2105–2128. [[CrossRef](#)]
32. Schneider, J.; Grosse, G.; Wagner, D. Land cover classification of tundra environments in the Arctic Lena Delta based on Landsat 7 ETM+ data and its application for upscaling of methane emissions. *Remote Sens. Environ.* **2009**, *113*, 380–391. [[CrossRef](#)]
33. Wessel, B. *TanDEM-X Ground Segment–DEM Products Specification Document*; Technique Note 3.1; Ger. Aerosp. Center (DLR): Wessling, German, 2016.
34. Rizzoli, P.; Martone, M.; Gonzalez, C.; Wecklich, C.; Borla Tridon, D.; Bräutigam, B.; Bachmann, M.; Schulze, D.; Fritz, T.; Huber, M.; et al. Generation and performance assessment of the global TanDEM-X digital elevation model. *ISPRS J. Photogramm. Remote Sens.* **2017**, *132*, 119–139. [[CrossRef](#)]
35. Oveisgharan, S.; Zebker, H.A. Estimating snow accumulation from InSAR correlation observations. *IEEE Trans. Geosci. Remote Sens.* **2007**, *45*, 10–20. [[CrossRef](#)]
36. Rosen, P.A.; Gurrola, E.; Sacco, G.F.; Zebker, H. The InSAR scientific computing environment. In Proceedings of the EUSAR 2012; 9th European Conference on Synthetic Aperture Radar, Nuremberg, Germany, 23–26 April 2012; pp. 730–733.
37. Chen, C.W.; Zebker, H.A. Two-dimensional phase unwrapping with use of statistical models for cost functions in nonlinear optimization. *J. Opt. Soc. Am. A* **2001**, *18*, 338–351. [[CrossRef](#)]
38. Berardino, P.; Fornaro, G.; Lanari, R.; Sansosti, E. A new algorithm for surface deformation monitoring based on small baseline differential SAR interferograms. *IEEE Trans. Geosci. Remote Sens.* **2002**, *40*, 2375–2383. [[CrossRef](#)]

39. Agram, P.S.; Jolivet, R.; Riel, B.; Lin, Y.N.; Simons, M.; Hetland, E.; Doin, M.P.; Lasserre, C. New Radar Interferometric Time Series Analysis Toolbox Released. *Eos Trans. Am. Geophys. Union* **2013**, *94*, 69–70. [[CrossRef](#)]
40. Biggs, J.; Wright, T.; Lu, Z.; Parsons, B. Multi-interferogram method for measuring interseismic deformation: Denali Fault, Alaska. *Geophys. J. Int.* **2007**, *170*, 1165–1179. [[CrossRef](#)]
41. Mackay, J.R. Downward water movement into frozen ground, western arctic coast, Canada. *Can. J. Earth Sci.* **1983**, *20*, 120–134. [[CrossRef](#)]
42. Zwieback, S.; Hensley, S.; Hajnsek, I. Assessment of soil moisture effects on L-band radar interferometry. *Remote Sens. Environ.* **2015**, *164*, 77–89. [[CrossRef](#)]
43. Lin, H.; Li, G.; Cuo, L.; Hooper, A.; Ye, Q. A decreasing glacier mass balance gradient from the edge of the Upper Tarim Basin to the Karakoram during 2000–2014. *Sci. Rep.-UK* **2017**, *7*, 6712. [[CrossRef](#)] [[PubMed](#)]



© 2018 by the authors. Licensee MDPI, Basel, Switzerland. This article is an open access article distributed under the terms and conditions of the Creative Commons Attribution (CC BY) license (<http://creativecommons.org/licenses/by/4.0/>).